



Original Paper

Molecular insight into the oil displacement mechanism of CO₂ flooding in the nanopores of shale oil reservoir



Xiao-Hu Dong ^{a, b, *}, Wen-Jing Xu ^{a, b}, Hui-Qing Liu ^{a, b}, Zhang-Xing Chen ^c, Ning Lu ^{a, b}

^a State Key Laboratory of Petroleum Resources and Engineering, China University of Petroleum, Beijing, 102249, China

^b MOE Key Laboratory of Petroleum Engineering, China University of Petroleum, Beijing, 102249, China

^c Department of Chemical and Petroleum Engineering, University of Calgary, Calgary, Alberta, T2N 1N4, Canada

ARTICLE INFO

Article history:

Received 23 May 2023

Received in revised form

4 August 2023

Accepted 7 August 2023

Available online 7 August 2023

Edited by Yan-Hua Sun

Keywords:

Displacement behavior

Nanopores

NEMD simulation

Shale oil

CO₂

Kerogen

ABSTRACT

With the increasing demand for petroleum, shale oil with considerable reserves has become an important part of global oil resources. The shale oil reservoir has a large number of nanopores and a complicated mineral composition, and the effect of nanopore confinement and pore type usually makes the effective development of shale oil challenging. For a shale oil reservoir, CO₂ flooding can effectively reduce the oil viscosity and improve the reservoir properties, which can thus improve the recovery performance. In this study, the method of non-equilibrium molecular dynamics (NEMD) simulation is used to simulate the CO₂ flooding process in the nanoscale pores of shale oil reservoir. The performance difference between the organic kerogen slit nanopore and four types of inorganic nanopores is discussed. Thus, the effects of nanopore type and displacement velocity on the nanoscale displacement behavior of CO₂ are analyzed. Results indicate that the CO₂ flooding process of different inorganic pores is different. In comparison, the displacement efficiency of light oil components is higher, and the transport distance is longer. The intermolecular interaction can significantly affect the CO₂ displacement behavior in nanopores. The CO₂ displacement efficiency is shown as montmorillonite, feldspar > quartz > calcite > kerogen. On the other hand, it is found that a lower displacement velocity can benefit the miscibility process between alkane and CO₂, which is conducive to the overall displacement process of CO₂. The displacement efficiency can significantly decrease with the increase in displacement velocity. But once the displacement velocity is very high, the strong driving force can promote the alkane to move forward, and the displacement efficiency will recover slightly. This study further reveals the microscopic oil displacement mechanism of CO₂ in shale nanopores, which is of great significance for the effective development of shale oil reservoirs by using the method of CO₂ injection.

© 2023 The Authors. Publishing services by Elsevier B.V. on behalf of KeAi Communications Co. Ltd. This is an open access article under the CC BY-NC-ND license (<http://creativecommons.org/licenses/by-nc-nd/4.0/>).

1. Introduction

As a type of unconventional energy with abundant reserves, the effective development of shale oil is essential to ensure world energy supply. The success of the shale oil revolution in the United States has greatly improved the self-sufficiency of crude oil in United States, and has focused the world's attention on shale oil resources (Yang and Jin, 2019). However, the reservoir properties of shale oil vary greatly compared with the conventional reservoirs. On the one hand, the pore scale space of shale reservoir is very

small, mainly composed of nanopores, and microscale and millimeter pores only develop locally (Loucks et al., 2009; Feng et al., 2020). Due to the narrow flow channel and the comparability between pore size and fluid size, the fluid transportation behavior in nanopores is easily affected by the porewall surfaces. Specifically, with the pore size decreases, the confinement effect of porewall on fluid in the pore is significantly enhanced (Wang et al., 2014; Liu and Zhang, 2019). On the other hand, the mineral composition of shale rocks is also complicated, which contains rich organic matter and a variety of inorganic minerals. The inorganic minerals mainly include clay minerals (e.g., kaolinite, illite and montmorillonite), carbonate minerals (calcite, dolomite) and quartz (silica) (Shaw and Weaver, 1965; Han et al., 2022). Simultaneously, fluid transportation behavior is also greatly affected by the mineral

* Corresponding author. State Key Laboratory of Petroleum Resources and Engineering, China University of Petroleum, Beijing, 102249, China.

E-mail address: dongxh@cup.edu.cn (X.-H. Dong).

composition because of the apparent interaction between different types of minerals and fluids. Compared with the conventional petroleum reservoirs, an effective development of shale oil reservoir is more difficult. But, in decades, with the development of horizontal well and volume fracturing technologies, the petroleum production from shale oil has increased rapidly in the world (Chaudhary et al., 2011). However, the commonly-used development mode of natural depletion for shale oil reservoirs gradually faces the problems of low single well productivity, rapid oil production declining, and low recovery factor (5%–10%) (Liu et al., 2022a). Therefore, it is urgent to propose a new development mode which can effectively improve the recovery performance of shale oil reservoir.

Researchers have proposed a number of enhanced oil recovery (EOR) technologies, e.g., miscible gas injection, chemical flooding, carbonized water flooding and thermal recovery technologies etc. (Agi et al., 2020; Zhou et al., 2022). Although most of them have been widely applied in the conventional oil fields, considering the unique properties of shale oil reservoir, an effective EOR technology is still challenging. In recent decades, some experimental and simulation runs have been performed on the EOR processes of shale oil reservoir, e.g., CO₂ flooding, chemical flooding (Liu and Zhang, 2019; Feng et al., 2020; Zhang et al., 2020). Compared with the other additives, CO₂ is one of the most potential mediums, which can efficiently enter the small-scale pores of shale rocks. Then, under the mechanisms of reducing oil viscosity, enhancing reservoir energy and improving oil flowability, the recovery performance can be significantly improved (Jia et al., 2019; Wei et al., 2020). At present, a series of laboratory experiments and numerical simulation runs have been conducted on the CO₂ injection process in shale reservoirs (Liu et al., 2022b; Hoffman and Shoib, 2014; Li et al., 2021). Typically, Kovscek et al. (2008) analyzed the CO₂ displacement process in siliceous shale rocks and discussed the influence of CO₂ miscibility on the displacement efficiency of shale oil. They found that under a near miscible condition, the recovery factor of shale oil can be increased by using a countercurrent mode than a cocurrent flow mode. Fan et al. (2022) conducted a continuous multi-pressure point displacement experiment (progressive displacement) with nuclear magnetic resonance technology to simulate the actual continuous CO₂ displacement process of shale reservoirs. Their results indicated that the displacement state was changed from an immiscible displacement to a near miscible displacement and then to a miscible displacement with the increases in pressure. The cumulative oil recovery factor can exhibit a step-like growth trend under the continuous multi-pressure point displacement process, and the increases in recovery efficiency can decrease in turn under a different displacement condition. Huang et al. (2023) conducted the comparative tests between pure CO₂ flooding and dimethyl ether (DME) assisted CO₂ flooding for shale oil reservoirs. Simultaneously, they also analyzed the microscopic recovery characteristics of different injection methods. From their observation, the shale rocks can be classified into three types (type I, type II and type III) and their corresponding physical properties, pore throat structures and percolation capacities were decreased successively. Compared with a CO₂ flooding process, a DME assisted CO₂ flooding can present a higher recovery factor. Meanwhile, this new hybrid recovery process is more pressure-sensitive, and with the pressure increases, the recovery factor can be increased more significantly. On the other hand, based on a group of numerical simulation runs, Wang et al. (2010) evaluated the enhanced oil recovery (EOR) potential of CO₂ flooding in Bakken shale oil reservoirs. Their results indicated that a continuous CO₂ flooding after the primary recovery process is the most effective method to improve the oil recovery velocity and injection capacity. Zhou et al. (2019) compared three CO₂ flooding technologies through

experimental and numerical simulation methods, and analyzed the influence of various parameters on the performance of CO₂ flooding process. Simultaneously, the injection velocity and well pattern of the target reservoir is also optimized. Aiming at a shale oil block in Elm Coulee oilfield, Xu and Hoffman (2013) compared the difference of the recovery performance of transverse hydraulic fractures wells and longitudinal hydraulic fractures wells. Then, they determined the breakthrough time, total oil production and final recovery factor of CO₂ flooding from different hydraulic fractures in the reservoir. They also provided a comparison to find the optimal direction of hydraulic fracturing. Although the above studies provided a large number of important data to understand the CO₂ displacement process in shale oil reservoirs, it is still unclear on the interaction mechanisms between CO₂ and oil in the shale nanopores by using the existing experimental and numerical simulation techniques. The particularity of shale rocks indicates the importance of studying the displacement regulation of CO₂ in nanoscale pores. In addition, the performance of a CO₂ injection process is highly sensitive to the reservoir properties and the complexity of shale pores, which brings a great uncertainty for the performance of a CO₂ displacement process (Safi et al., 2016; Fang et al., 2017). Therefore, in order to achieve the effective development of shale oil reservoir, it is urgent to figure out the CO₂ displacement mechanism on the nanoscale level.

Molecular dynamics (MD) simulation, as an effective technique to study the microcosmic world from the molecular and atomic levels, can be applied to address the hydrodynamics and thermodynamic properties in the nanopores of oil reservoirs (Dong et al., 2022; Li et al., 2022; Wang et al., 2016a). Sun et al. (2023) applied the method of MD simulation to study the displacement behavior of CO₂ to methane and discussed the effects of depressurization exploitation and injection pressure on the displacement behavior. They classified the CO₂-CH₄ displacement behavior into three stages, including CH₄ reverse flow stage, injection pressure action stage, and positive displacement stage. Zhang et al. (2020) simulated the dynamic transportation process of oil with different methane fractions through a quartz nanopore throat. They found that the dissolution of methane can provide a positive effect on the movement of crude oil in the nanopore throat. Fang et al. (2020) characterized the miscibility and displacement behavior of CO₂/oil system in three kinds of inorganic slit nanopores by using the MD simulation method. It was showed that the stability of displacement front is very important to ensure a smooth transportation process of oil phase. In addition, the mineralogy and oil composition were also significant for the miscibility state and displacement process of CO₂ flooding. Liu et al. (2017) applied the non-equilibrium molecular dynamics (NEMD) simulation method to study the displacement behavior of CO₂ on dodecane. They found that the injected CO₂ can preferentially adsorb in the proximity of the porewall surface and form a layering structure because of the hydrogen bonds interaction between CO₂ and the hydroxyl (–OH) groups of inorganic porewall. Yan et al. (2017) simulated the displacement behavior of the injection method of alternating H₂O/CO₂ in the quartz slit nanopore of shale oil. They found that the two different injection fluids can induce a synergistic effect, CO₂ can effectively dissolve the polar oil components from the porewall surface, and H₂O can benefit the stable displacement velocity. Xiong et al. (2021) used *n*-decane to represent shale crude oil and simulated the displacement behavior of four types of injected gases (CO₂, CH₄, N₂ and C₃H₈). The results indicated that the injected gases exhibit great advantage in deep reservoir than that in shallow reservoir, and CO₂ has the strongest displacement ability. Based on the discussion above, it can be found that the current investigations about the CO₂ displacement behavior and mechanisms in shale nanopores are still insufficient. In most studies, the shale oil is just

simplified as a single oil component model, which is significantly different from the actual composition of shale oil. Simultaneously, as another important factor to dominate the oil displacement behavior in shale rocks, a good understanding on the effect of nanopore type is also required.

In order to address the above requirements, this study performs a series of MD simulation runs for the CO₂ displacement process of shale nanoscale pores through a NEMD simulation method. Then, based on the simulation results, the effect of displacement velocity and nanopore type on the CO₂ displacement behavior in shale oil reservoirs are analyzed. In Section 2, a kerogen organic pore displacement model and four different inorganic pore displacement models are firstly developed. And the specific simulation details are also provided. In Section 3, we conducted a series of MD simulations to analyze the displacement process of CO₂ in the five types of nanopore models, and investigated the displacement performance of CO₂-shale oil under different conditions. Specifically, the parameters of fluid density distribution, fluid transport distance, interaction energy and displacement efficiency are calculated and used as the evaluation indicators. In addition, the effect of displacement velocity on the CO₂ displacement process in nanopores is also studied. In the last section, the main conclusion remarks are presented.

2. Molecular models and simulation methods

2.1. Organic slit pore model

Organic matter is the storage and transport space of shale oil and gas. It indicates that it is very important to explore the displacement behavior of CO₂ and shale oil in organic pores. In decades, considering the carbon-based properties and pore structure characteristics of shale organic matter, a large number of MD simulations applied some simply organic nanopores to represent the shale organic nanopores, e.g., carbon nanochannels, multilayer graphene plate slits (Meyer et al., 2007), carbon nanotubes (CNTs) (Chen et al., 2021) and crystal-arranged carbon atom plates (Chen et al., 2017) etc. These nanopore models can be used for equilibrium molecular dynamics (EMD) simulation to characterize the adsorption and diffusion characteristics of fluid in shale nanopores (Wang et al., 2015; Zhang et al., 2019; Li et al., 2019). But for NEMD simulation runs, the simplified nanopore model is not enough to satisfy the research requirements of characterizing the fluid transportation behavior with driving force. Yu et al. (2020a) and Wu and Zhang (2016) investigated the flow characteristics of hydrocarbon gases in graphene nanopores by NEMD simulation. From their simulation results, an obvious slippage behavior can be found at the porewall surface, while no slip flow was found in the inorganic nanopores under the same conditions. The phenomenon is inconsistent with the real reservoir performance and contradicts with the conclusions of some studies (Zhang et al., 2017, 2019). In the study of potential energy surface of the porewall, it is found that the slippage phenomenon does not depend on the interaction force between gas and porewall, but is related with the roughness of porewall surface. Because of the simplified structure and smooth surface of graphene wall, it is difficult to represent the real transport characteristics of the organic nanopores. Therefore, it is necessary to develop a porewall model which can realistically represent the characteristics of irregular organic nanopores in shale rocks. In recent years, the kerogen nanopore model with a complicated composition and structure are commonly used to simulate the fluid flow behavior in organic pores.

With the continuous investigation on the organic matter of shale rocks, its organic composition has been described detailedly by the experimental means, e.g., X-ray photoelectron spectroscopy

(XPS) (Canneva et al., 2017), nuclear magnetic resonance (Wang et al., 2016b) and some other experimental methods (Feng et al., 2020). The organic matter of shale is mainly composed of kerogen, and its main elements include hydrogen and oxygen, with a small amount of the elements of nitrogen and sulfur. From the microscopic point of view, the structural distribution of kerogen molecules is complex and the bonding modes of each atom in kerogen molecules are varied. Depending on the number of C–H bonds and the number of C–O bonds, kerogen molecules usually show a ring or chain structure. Yu et al. (2020b) simulated the flow behavior of methane in three classical kerogen nanopores (2–8 nm). Their results showed that under different pressure and temperature conditions, the fluid in nanopores always showed the non-slip flow characteristics, and the flow behavior was consistent with the continuous flow theory (N–S equation). Therefore, it is reasonable to use a kerogen model to characterize the organic pores in NEMD simulation for fluid flow problem. At present, scholars have proposed the kerogen models with different element ratios and molecular structures based on the organic matter samples extracted from different types of shale reservoirs (Bousige et al., 2016; Wang et al., 2019). Ungerer et al. (2015) established a series of representative kerogen unit models by combining the thermodynamic parameters obtained from the atomic mechanics and the volume characteristics obtained from the molecular dynamics, which shows a good agreement with the experimental results. The proposed II-C kerogen unit (C₂₄₂H₂₁₉O₁₃N₅S₂) has a high maturity, which is used to represent the kerogen model formed in the middle stage of a shale reservoir and meets the requirement of this study, as shown in Fig. 1.

Spatial data of the kerogen molecular model are obtained and the consistent valence force field (CVFF) is applied to the kerogen units (Dauber-Osguthorpe et al., 1988). It is necessary to optimize the configuration of kerogen molecules to construct the long plate kerogen slit pore model required for simulation. The simulation process is shown in Fig. 2. First, a simulated box with a large initial size of 22 × 5.2 × 10 nm³ is set up, and 24 kerogen molecules are evenly arranged in the simulated box. The NVT ensemble (a constant particle number N, constant volume V and a temperature fluctuating around an equilibrium value) is set in the system, and the initial temperature is set as 330 K and the maximum temperature is set as 900 K. After a series of annealing simulations, the

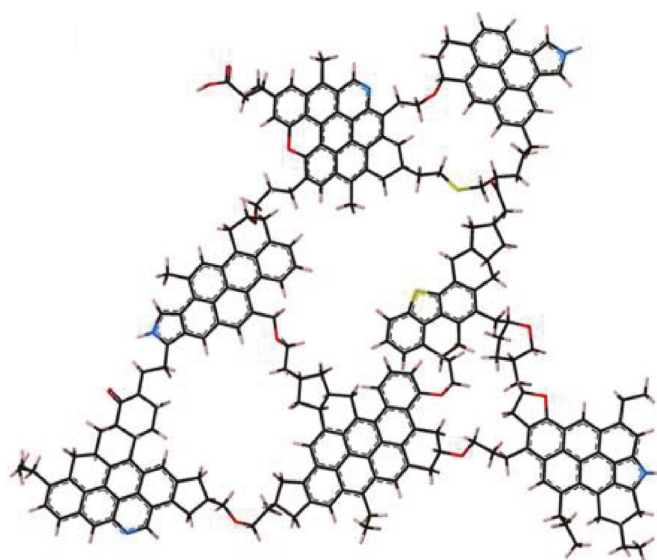


Fig. 1. Type II-C kerogen unit (Ungerer et al., 2015).

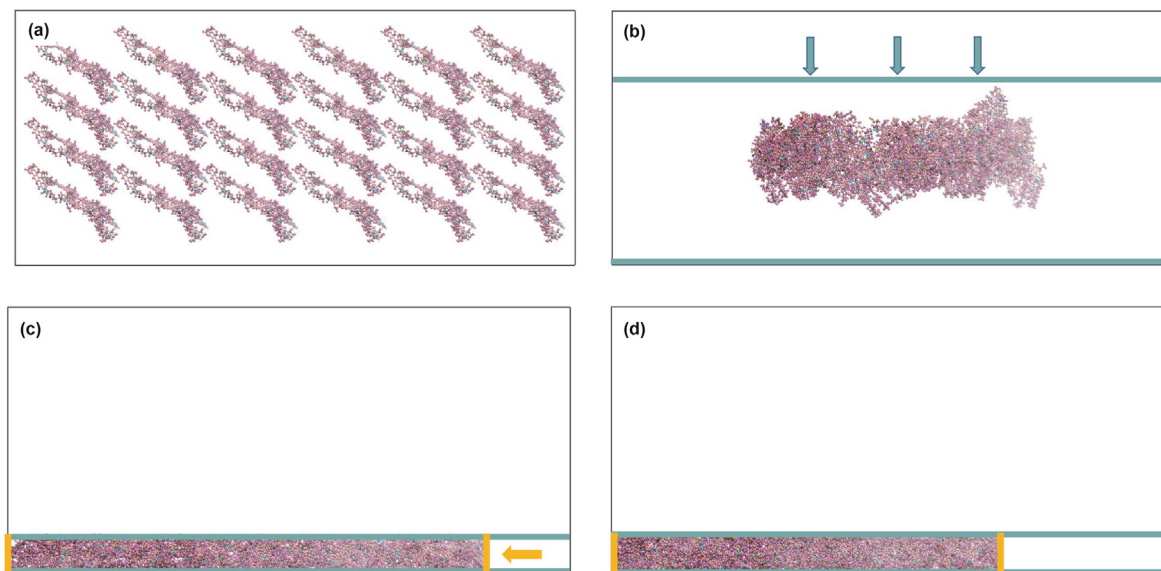


Fig. 2. Construction process of the kerogen porewall model.

structure of the kerogen molecules tends to be stable and the system reaches the equilibrium status. Then, the LJ (Lennard-Jones) potential energy walls are set at the top and bottom of the z direction of this system, which only retain the repulsive effect on kerogen molecules to reduce the influence on the structure of kerogen. The lower wall is fixed to be stationary, and the upper wall moves vertically and slowly downwards. Then, the kerogen cluster is compressed longitudinally, and the movement is terminated once the upper wall moves to the location of $z = 1.5$ nm. Then, the same operation is carried out in the x direction. LJ potential energy walls are set on the left and right sides of the x direction of this system. The left wall is fixed, and the right wall moves slowly to left, and the kerogen cluster is compressed laterally. When the right wall is moved to $x = 15$ nm, the wall is fixed. Finally, the structure of kerogen is basically stable after 500 ps simulation at 330 K, and the final configuration is shown in Fig. 2(d). The size of the whole block kerogen is about $15.0 \times 5.2 \times 1.5$ nm³. The density of the simulated II-C kerogen is calculated to be 1.19 g/cm³, which is consistent with the experimental density range of type II kerogen (1.18–1.35 g/cm³) (Ungerer et al., 2015).

Based on the obtained kerogen porewall model, a slit-like kerogen nanopore model with a width of 5 nm can be established, as shown in Fig. 3. Then, a CO₂ system box is added on the left side of kerogen nanopore. The size of this CO₂ box is

$9.15 \times 5.2 \times 8$ nm³. And thus, the CO₂ molecules are filled in this box according to the temperature and pressure conditions of 330 K and 30 MPa. Meanwhile, the kerogen nanopore is filled with a certain amount of shale oil molecules. For the shale oil components of this simulation model, an alkane mixture is applied to represent the oil fluid, which include methane (8 wt%), *n*-octane (42 wt%), and *n*-eicosane (50 wt%). Thereafter, a vacuum layer is set on the right side to avoid the effect of lateral periodic boundaries. A pressure plate is placed on the left side of CO₂ fluid, and the movement velocity of plate is set to provide the driving force for the fluids in nanopores.

2.2. Inorganic slit pore model

For the inorganic nanopore, four different inorganic porewall models of the shale rocks are established in this paper, including quartz, feldspar, calcite and montmorillonite porewall molecular models. A validation process for the different porewall models developed in this paper can be found in one of our previous publications (Dong et al., 2023). Therefore, four kinds of inorganic slit nanopore models of quartz, feldspar, calcite and montmorillonite can be developed.

First, α -SiO₂ is a common type of quartz crystals in nature. The crystal parameters a , b and c are 0.49965, 0.49965 and 0.5457 nm,

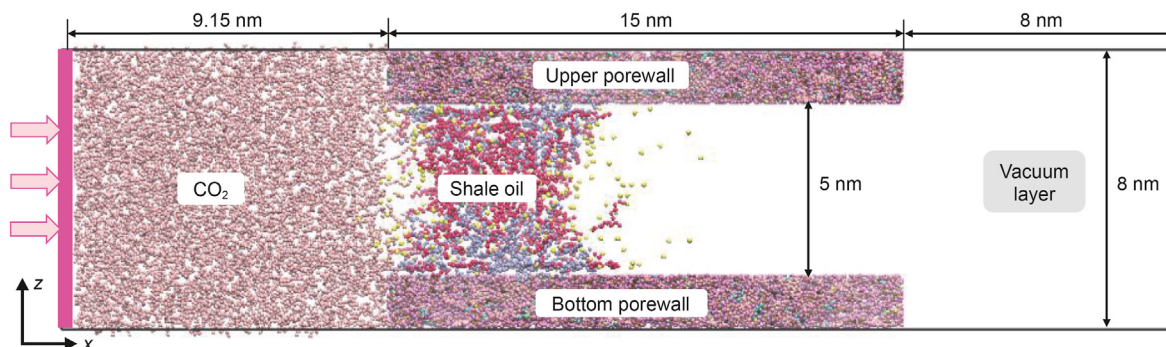


Fig. 3. Snapshot of the organic nanopore model (color code: yellow, methane; red, octane; blue, eicosane; pink, CO₂).

respectively. The angle parameters α , β and γ are 90° , 90° and 99° (Goumans et al., 2007). The crystal surface (1 0 0) is cut to obtain a stable crystal structure. The porewall surface is completely hydroxylated. The quartz mineral model is shown in Fig. 4(b), and the porewall size is $14.7 \times 5.2 \times 1.4 \text{ nm}^3$. Then, the molecular formula of K-feldspar is KAlSi_3O_8 , which belongs to the monoclinic crystal system. This crystal system consists of Al–O and Si–O tetrahedra, each one centered on an Al or Si metal ion and sharing four oxygen atoms with the surrounding tetrahedra, and the metal ion K^+ is located in the structure of the tetrahedra to balance the negative charge (Soni and Patey, 2019). For this crystal system, the common crystal surface (0 0 1) is selected to cut (Kerisit and Liu, 2012), and the porewall surface of feldspar is also hydroxylated. The porewall size of feldspar mineral model (Fig. 4(b)) is $14.5 \times 5.1 \times 1.6 \text{ nm}^3$. Third, the molecular formula of calcite crystal is CaCO_3 , which belongs to the trigonal crystal type. The crystal parameters a , b and c are 0.499, 0.499 and 1.706 nm. The angle parameters α , β and γ are 90° , 90° and 120° (Yang et al., 2008), and the space group is R-3c. The calcite crystal is cut along the (1 0 4) surface, and the porewall size (Fig. 4(b)) is $14.6 \times 5.0 \times 1.2 \text{ nm}^3$. Finally, montmorillonite is a 2:1 clay mineral. When there are two Si–O tetrahedral, it will be an Al–O octahedral at the same time (Hu et al., 2014). Na-montmorillonite is a common type in shale. It belongs to the monoclinic system. And the molecular formula is $\text{Na}_{0.75}(\text{Al}_{0.25}\text{Si}_{7.75})(\text{Al}_{3.5}\text{Mg}_{0.5})\text{O}_{20}(\text{OH})_4$. The crystal parameters a , b and c are 0.523, 0.906 and 0.960 nm. The angle parameters α , β and γ are 90° , 90° and 99° . The space group is C2/m. The model is cut along the (0 0 1) surface, and the size of porewall model is $14.7 \times 5.3 \times 1.5 \text{ nm}^3$. The model structure is shown in Fig. 4(b).

The size settings and simulation parameters of the inorganic nanopore model are consistent with the kerogen organic nanopore model developed in Section 2.1. Similarly, a slit-like nanopore model with the width of 5 nm is established and it is also filled with the fluid molecules. The developed inorganic nanopore model is shown in Fig. 4(a).

2.3. Simulation details

Molecular force field, also known as potential function, is usually applied to calculate the interparticle force in MD simulation runs, which needs to ensure a good computational efficiency and a high computational accuracy. Generally, the total potential energy can be expressed as the sum of four potential energies:

$$E_{\text{total}} = E_{\text{bonds}} + E_{\text{angles}} + E_{\text{dihedrals}} + E_{\text{nonbonded}} \quad (1)$$

where E_{total} is the total potential energy, kcal/mol, which includes bond energy E_{bonds} , angle energy E_{angles} and dihedral angle energy $E_{\text{dihedrals}}$, as well as non-bonded potential energy $E_{\text{nonbonded}}$ of van der Waals interaction and charge interaction. The differences between force field models are reflected in the specific forms of functions and parameters of force fields. For OPLS force field, each potential energy term can be expressed as:

$$E_{\text{bonds}} = \sum_{\text{bonds}} K_r (r - r_0)^2 \quad (2)$$

$$E_{\text{angles}} = \sum_{\text{angles}} K_\theta (\theta - \theta_0)^2 \quad (3)$$

$$E_{\text{dihedrals}} = \frac{c_1}{2} [1 + \cos(\varphi)] + \frac{c_2}{2} [1 + \cos(2\varphi)] + \frac{c_3}{2} [1 + \cos(3\varphi)] + \frac{c_4}{2} [1 + \cos(4\varphi)] \quad (4)$$

$$E_{\text{nonbonded}} = \sum_{i>j} \left\{ 4\epsilon_{ij} f_{ij} \left[\left(\frac{\sigma_{ij}}{r_{ij}} \right)^{12} - \left(\frac{\sigma_{ij}}{r_{ij}} \right)^6 \right] + \frac{q_i q_j e^2}{r_{ij}} \right\}, r < r_{\text{cut}} \quad (5)$$

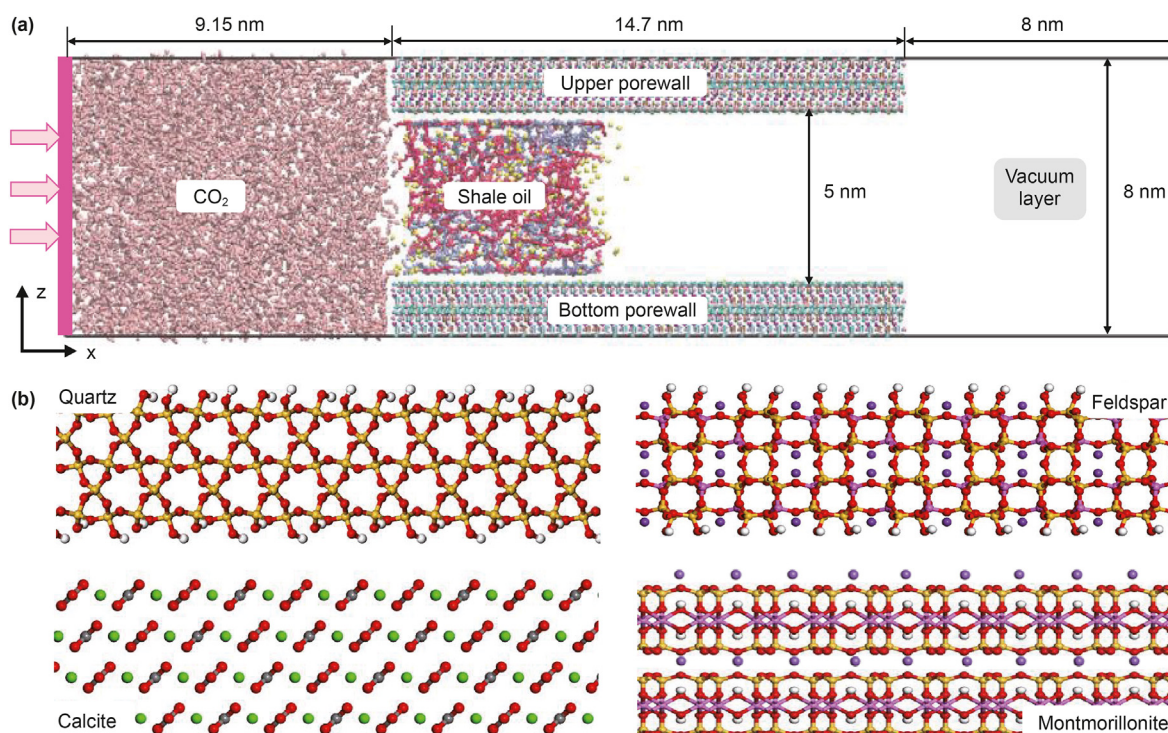


Fig. 4. (a) Snapshot of the inorganic nanopore model, taking the montmorillonite porewall as an example; (b) Porewall structures of four types of inorganic minerals.

In this study, a TraPPE (transferable potential for phase equilibrium) force field is used for CO₂ fluid, in which CO₂ molecules have rigid constraints and no intramolecular interactions (Liu and Wilcox, 2012). A OPLS (optimized force field for liquid simulations) force field is used to simulate the potential energy of shale oil fluids, which is highly reliable for simulating the thermodynamic properties of small organic molecules (Jorgensen et al., 1984). The united atom force field (OPLS-UA) is adopted to represent methane (CH₄), methyl (–CH₃) and methylene (–CH₂) by a single atom (Etha et al., 2021), which not only ensures a high computational accuracy but also improves the simulation efficiency. For the four types of inorganic pore models, calcite porewall is calculated by using the potential function equation established by Xiao et al. (2011), which simplified the calculation process by using the LJ potential function instead of the Buckingham potential function for the force field. In this study, the quartz, montmorillonite, and feldspar porewalls are described by using the ClayFF model. For inorganic minerals, the ClayFF is one of the most commonly-used models. Compared with the results of first principles, it has a high consistency and can well predict the adsorption isotherms of small molecules alkanes on the inorganic porewalls (Cygan et al., 2004). For the interaction parameters between different atoms, the Lorentz–Berthelot mixing rule is used, and the cutoff radius is set as 1.2 nm. The PPPM (particle–particle–particle–mesh) algorithm is used to calculate the long-range electrostatic force.

For all the MD simulation runs in this paper, the open source software LAMMPS is applied (Prieve and Russel, 1988). Before simulating the displacement process, a 1 ns equilibrium simulation run is firstly carried out for alkanes in nanopores under a NVT ensemble to simulate the effect of alkanes adsorption behavior in the real reservoir pores. Then the displacement speed can be set through the pressure plate on the left side of CO₂ fluid. It can drive the shale oil in the slit-like nanopore along the direction of *x* axis (right front). The system temperature is always set as 330 K and the time step is set to 1 fs. And the data analysis is recorded every 1000 steps.

3. Results & discussion

In this section, the results of MD simulation runs for the CO₂ displacement process in five different types of shale nanopore models are discussed. Simultaneously, the effect of CO₂ displacement velocity is also discussed. In this process, from the results of fluid density distribution and interaction energy, the displacement mechanism of CO₂ at nanoscale pores for the shale oil reservoirs can be obtained.

3.1. Oil displacement behavior in inorganic nanopores

Firstly, the MD simulation results of CO₂ in the four inorganic nanopores are discussed. In these cases, the displacement velocity is set as 4 m/s, and the fluid movement behavior within 2 ns is discussed. The motion states of fluid molecules during the displacement process are shown in Fig. 5. Based on the snapshots, the displacement characteristics can be intuitively analyzed. At the initial stage of displacement process, the CO₂ molecules advances forward and gradually dissociates the alkane molecules adsorbed on the porewall surfaces. From Fig. 5, it can be observed that for the porewall surfaces of feldspar and montmorillonite, only a small amount of alkanes remain after the displacement process. It indicates that CO₂ has a large capacity to separate and displace the alkanes on these porewall models. Simultaneously, the CO₂ displacement phase in the both nanopore models also shows a stable displacement front and a large displacement distance. In contrast, for calcite and quartz porewall surfaces, it can be found

that the molecules of octane and eicosane are attached on the porewall surfaces, and an oil adsorption film can be observed forming on the left side of the porewall models. It impedes the forward advance of CO₂ around the porewall surfaces and has a negative effect on the displacement of alkanes in the pores. With the displacement process continues, the difference of displacing phenomena in pores increase further. The total number of alkane molecules attached on the calcite porewall surface is increased, and meanwhile, the CO₂ molecules tends to accumulated in the pore center. This phenomenon can result in the continuous breakthrough of displacement front. Thus, a channeling behavior of CO₂ molecules can be observed. It indicates that an ineffective displacement process has been reached for the subsequent CO₂ molecules. On the other hand, it can be also found that among the four different nanopore models, the CO₂ molecules in the montmorillonite nanopore shows a higher displacement speed, and the CO₂ molecules in this case reaches the outlet of nanopore firstly. The CO₂ fluid displacement state in the feldspar pore is stable, and the residual amount of alkane on the porewall is the least, so the shape change of the displacement front in the feldspar pore is the least. Compared with the first two types of pores, the residual oil on the porewall of quartz pores is the most, and the displacement effect is slightly poor.

Fig. 6 provides the density distributions of octane and eicosane along the *x* direction at different displacement times. It can be found that with the displacement time increases, both the density peaks of octane and eicosane can move forward, this indicates that an effective displacement process has been developed. But the changing behavior for the densities of octane and eicosane is significantly different. In comparison, the density peak of octane is higher, and the changing process of its peak value is less affected by the displacement time. Simultaneously, the final density peak of octane is narrower in the *x* direction and closer to the nanopore outlet. This means that octane has a long transportation distance during the displacement process, and an effective displacement is obtained. But with the increase in displacement time, the density peak of eicosane becomes wider and its peak value decreases rapidly. Compared with octane, the shape of the density peak for eicosane is low and flat. Therefore, the residual eicosane on the surface of inorganic porewall is more widely distributed and abundant during the displacement process, and the displacement efficiency of CO₂ on eicosane is lower than that of octane.

On the other hand, from Fig. 6, it can be also observed that the displacement characteristics in the four different inorganic nanopores differ significantly. The displacement effect is relatively better for the nanopores of montmorillonite and feldspar, the peak densities of octane and eicosane at the end of the displacement process (2 ns) in these two types of pores are higher than those exhibited in calcite and quartz pores, and almost no residual alkane molecules is observed around the nanopore entrance (3 nm). The density peaks of the two alkanes for the montmorillonite nanopores can move closer to the outlet, which indicates that the transportation distance is higher. In contrast, the peak density of octane in the nanopores of calcite and quartz is lower, and some residual octane molecules can be observed from the pore inlet. Meanwhile, a more obvious distribution behavior can be also observed for eicosane. For the calcite nanopore, eicosane is difficult to find an obvious peak, and the density curve is approximately shaped as a trapezoidal state. Simultaneously, compared with octane, the transportation distance of eicosane molecules is obviously lower, and no eicosane molecules can be observed from the nanopore outlet.

Fig. 7 gives the interaction energies between different molecules at different times during the displacement process. It can benefit to understand the results of CO₂ displacement behavior in nanopores. Here, the interaction energy between shale oil and porewall surface

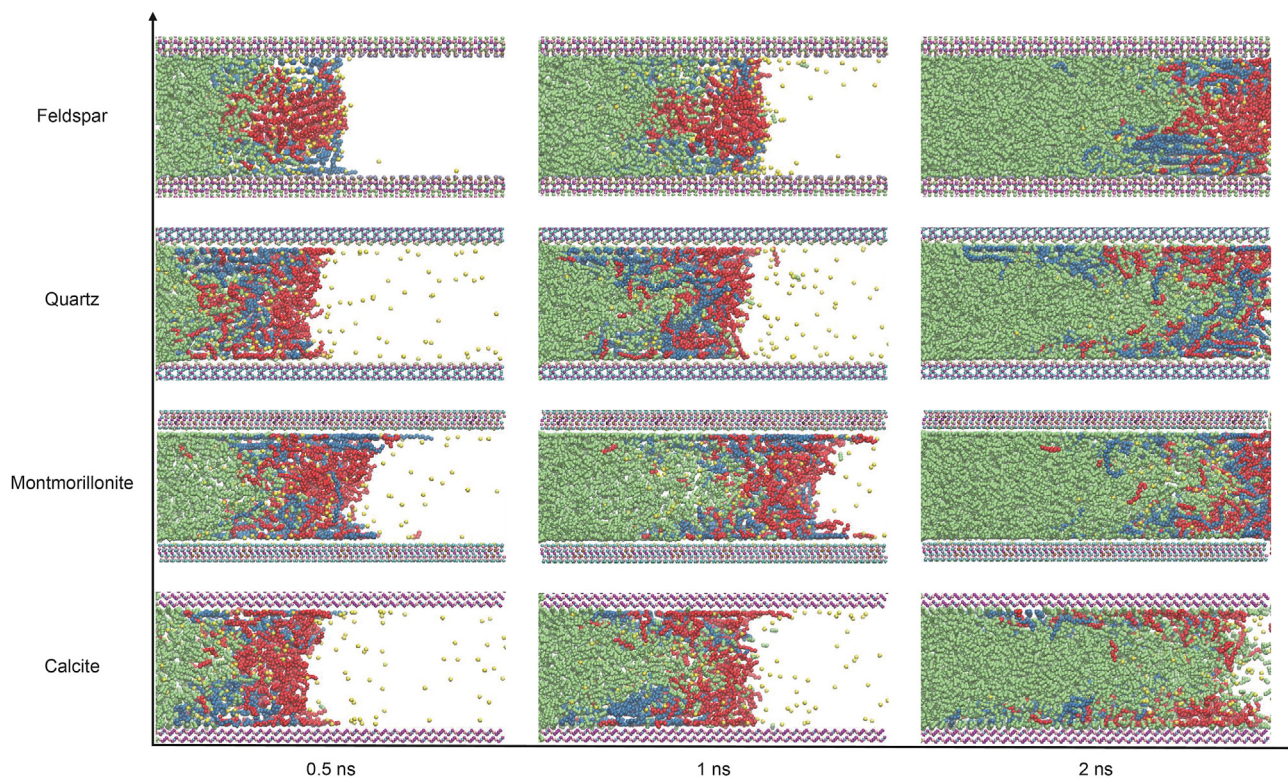


Fig. 5. Simulated snapshots in the four inorganic nanopores during the displacement process. The color markings are CO₂ (green), methane (yellow), octane (red), and eicosane (dark blue).

and the interaction energy between shale oil and CO₂ are mainly concerned. The former reflects the adsorption strength of porewall for fluid molecules. The larger $E_{\text{ALKANES-WALL}}$ is, the more easily alkane is adsorbed on the porewall surface and the more stable the adsorption state is. For a higher $E_{\text{ALKANES-WALL}}$ case, it is difficult for CO₂ to displace and separate alkanes adsorbed on the porewall surface, thus destroying the stability of the displacement interface. In contrast, the latter mainly represents the mixing ability of CO₂ and shale oil components. The larger $E_{\text{ALKANES-CO}_2}$ is, the more easily CO₂ and alkanes are miscible. It can result in a miscible displacement process, which is conducive to stabilize the displacement front. From Fig. 7, it can be found for the calcite nanopores, the value of $E_{\text{ALKANES-WALL}}$ is the highest, and $E_{\text{ALKANES-WALL}} > E_{\text{ALKANES-CO}_2}$, which leads to the formation of an alkane adsorption layer easily on the porewall surface. Therefore, a CO₂ fingering phenomenon can be observed, and thus the displacement efficiency is low. It also explains the formation mechanism of CO₂ gas channeling in the calcite nanopore in the late stage of the displacement process in Fig. 5. For the other three types of nanopores, the value of $E_{\text{ALKANES-CO}_2}$ is higher, which leads to a better displacement effect, and CO₂ fluid can always maintain slug displacement in the pores. In addition, from Fig. 7, it can be observed that $E_{\text{ALKANES-WALL}}$ in a feldspar nanopore is the smallest. Therefore, the adsorption strength of alkane molecules on the porewall surface is small. During the displacement process, the interaction between CO₂ and alkanes can play a dominant role. Simultaneously, from Fig. 5, it can be found that the displacement front of CO₂ in the feldspar nanopore is stable and the porewall surface has the least residual oil components.

3.2. Oil displacement behavior in organic nanopores

In this section, the MD simulation results of CO₂ in the organic

nanopores are discussed. The simulation conditions are consistent with that in the inorganic nanopores, and the displacement velocity is also set as 4 m/s. The motion states of fluid molecules during the displacement process are shown in Fig. 8. During the displacement process, CO₂ molecules can enter the nanopores with the push of pressure plate and drives shale oil molecules to move forward. During the displacement process, it can be observed that a large number of alkane molecules are still adsorbed on the porewall surface, and the displacement effect is not good. This oil film layer attached on the porewall surface are widely distributed from the inlet to the outlet. And compared with the results of the four inorganic nanopores in Fig. 5, the residual oil components on the kerogen organic porewall surface have the largest distribution. This also causes a serious ununiform of the flow velocity of CO₂ across the nanopore. Thus, the degree of gas fingering is aggravated, and finally the phenomenon of gas breakthrough can be observed (see Fig. 8(c)).

Fig. 9(a) shows the density distributions of octane and eicosane in the organic nanopore along the x direction. With the increase in displacement time, the peak density of octane decreases obviously. At the end of the displacement process (2 ns), the peak density of octane is only 0.16 g/cm³, and the peak density in the other four inorganic pores at the same moment is 0.18–0.30 g/cm³. The transport distance of octane in the pore is less than that in the four inorganic pores, and no octane molecules move to the exit end of the pore. The density variation of eicosane in the pore is similar to that in the calcite pore, with short displacement distance and more residual alkanes on the surface. The transport distance of this alkane fluid is expressed by calculating the change value of the center of mass (COM) of the alkane in the x direction, as shown in Fig. 9(b). A longer transport distance of fluid within the same time also represents a larger displacement velocity of the fluid caused by CO₂ in the pore. The transport distance of octane and eicosane in

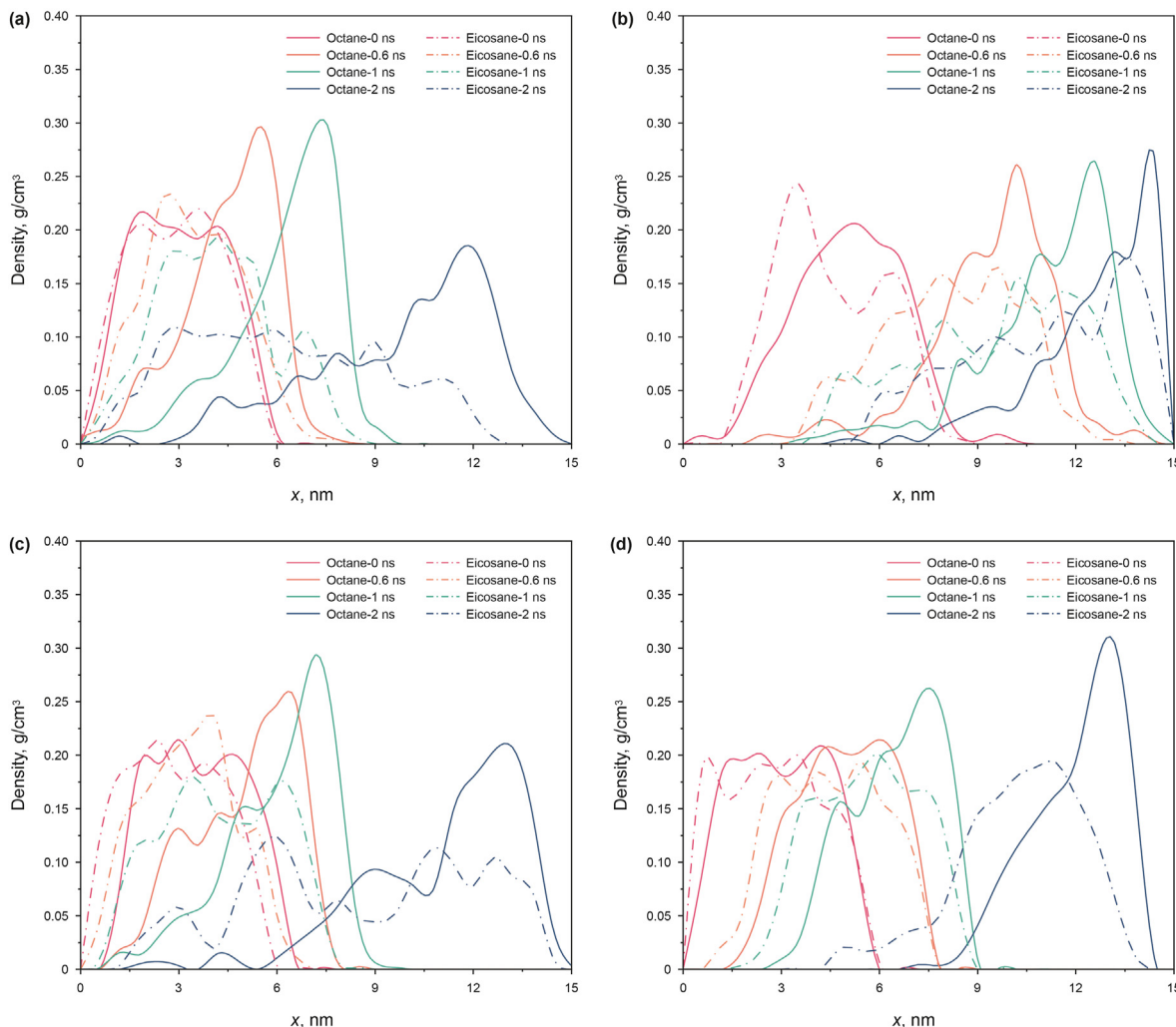


Fig. 6. Density distribution of alkanes. (a) Calcite; (b) Montmorillonite; (c) Quartz; (d) Feldspar.

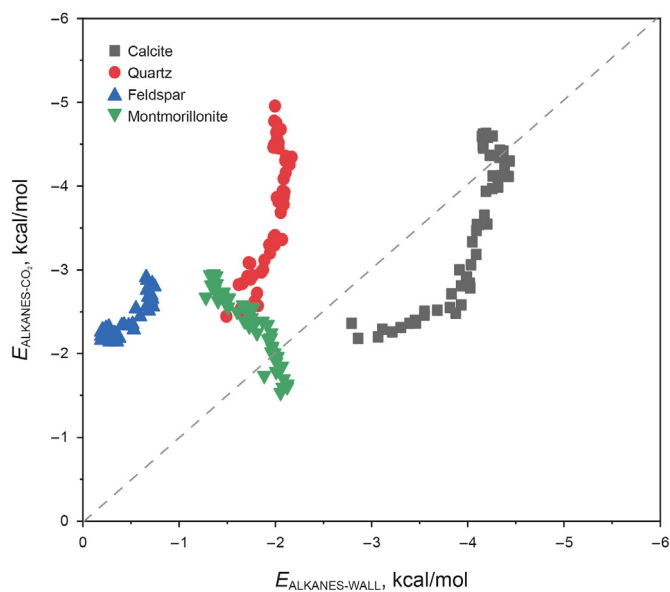


Fig. 7. Comparison of the interaction energy between shale oil and CO₂ and between shale oil and porewall surface.

kerogen pores is the shortest, while the transport distance of alkanes in the four inorganic pores is montmorillonite > feldspar > quartz > calcite, which is consistent with the analysis in Section 3.1. According to the above analysis, the displacement effect of CO₂ on alkanes in organic pores is obviously weaker than that in inorganic pores.

The interaction energies between shale oil and porewall and between shale oil and CO₂ in kerogen pores are calculated, and the results are shown in Fig. 10(a). It is found that the $E_{\text{ALKANES-WALL}}$ changes more with the increase in displacement time. It is because of the strong adsorption ability of the kerogen porewall to alkane, which leads to the continuous adsorption of alkane on the porewall. In the initial phase of displacement, the adsorption sites are usually occupied by eicosane with longer carbon chains. With the increase in the contact area between the alkane and the porewall, more octane can be adsorbed on the porewall. Therefore, it can be seen that the scatter is moving more and more to the $E_{\text{ALKANES-WALL}}$ side. Stronger $E_{\text{ALKANES-WALL}}$ and weaker $E_{\text{ALKANES-CO}_2}$ in the interaction energy resulted in poor displacement performance in the kerogen pore. The total CO₂-wall interaction energy in each pore is also calculated (Fig. 10(b)), which can represent the adsorption capacity of the porewall for CO₂. Compared with the four types of inorganic pores, the interaction energy between kerogen porewall and CO₂ is the smallest. This means that CO₂ is difficult to separate and desorb

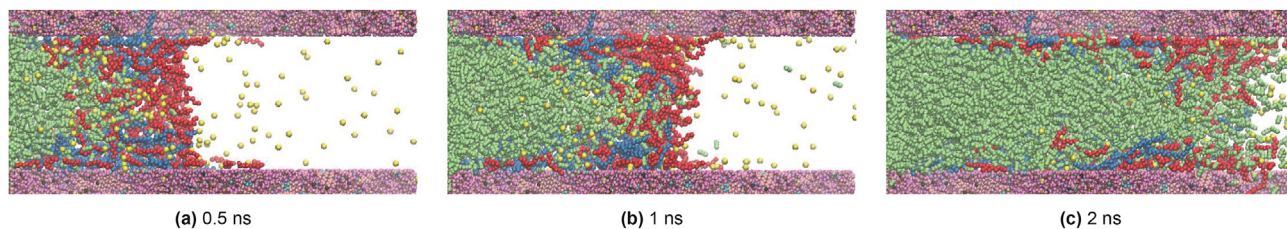


Fig. 8. Simulated snapshots in the organic nanopores during the displacement process. The color markings are CO₂ (green), methane (yellow), octane (red), and eicosane (dark blue).

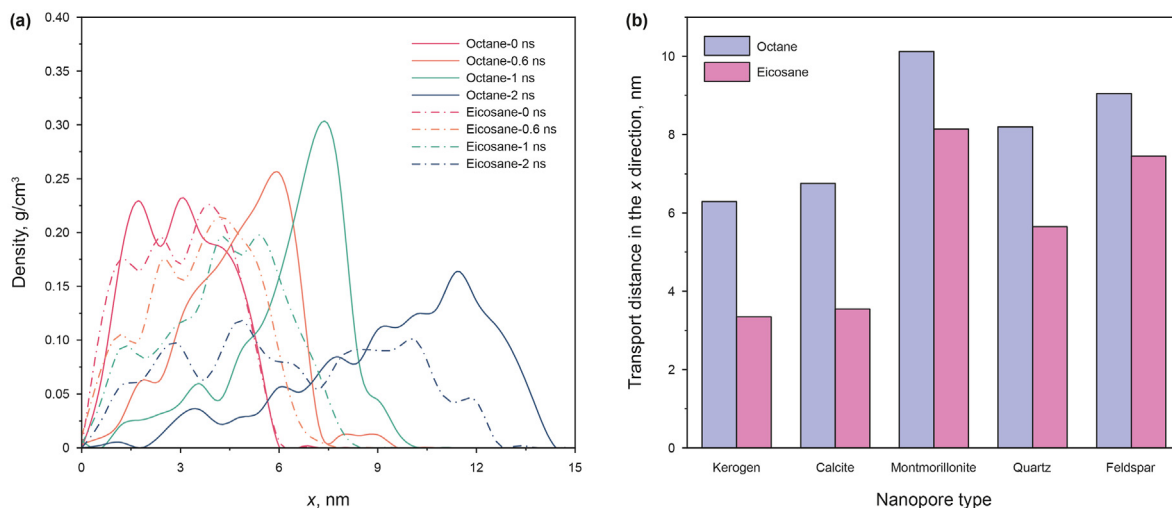


Fig. 9. (a) Density distributions of alkanes in the organic pore; (b) Transport distances of alkanes in the x direction.

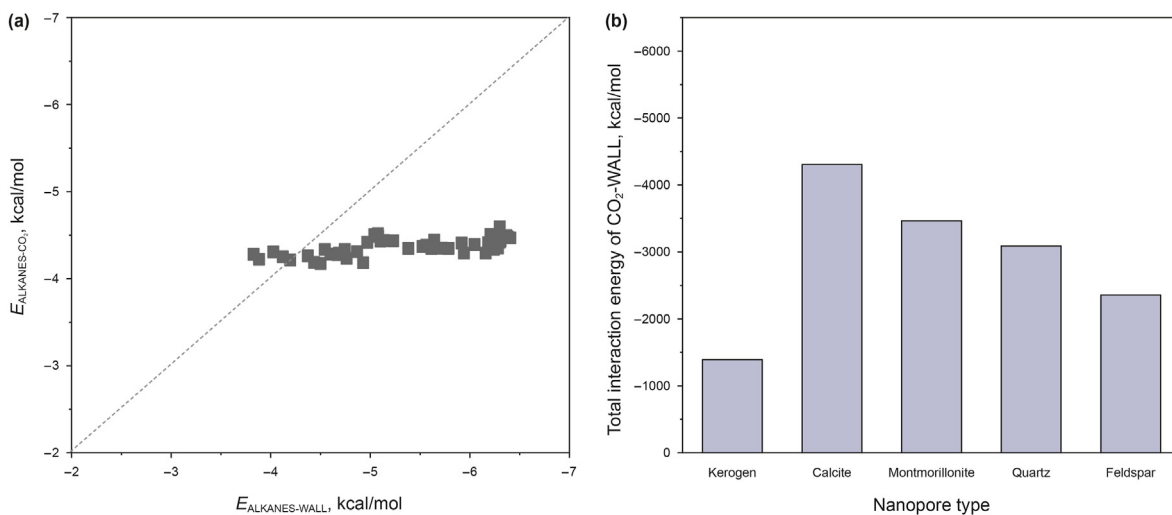


Fig. 10. (a) Comparison of interaction energies between shale oil and CO₂ and between shale oil and porewall surface in the system; (b) Total interaction energies between CO₂ and porewall surface.

alkanes from the kerogen porewall surfaces. However, the interaction energy of CO₂-wall cannot completely represent the displacement capacity of CO₂-wall. The calcite porewall has the highest interaction energy with CO₂. For static system, that is, when no driving force is applied, CO₂ has excellent displacement ability for alkanes after full contact with calcite porewall (Dong et al., 2023). However, under the action of external driving force, the contact time between CO₂ and the porewall is limited, so the

displacement performance of CO₂ on the adsorption of alkanes on the porewall is not satisfactory.

A quantitative index is set for CO₂ displacement capacity in different pores: the displacement efficiency, E_D , and the displacement behavior of CO₂ to shale oil can be described quantitatively by the displacement efficiency. The CO₂ displacement capacity can be expressed by the displacement transport length of the alkanes in the x direction. In the simulations, the pushing length of the

pressure plate used to provide driving force in the simulation is 8 nm, so the effective displacement of the alkanes is defined as the displacement distance equal to or greater than 8 nm. This means that the trajectories of the particles are counted in the COM, and if the particle moves no less than 8 nm in the x direction, the particle is identified as an effective displacement. The N_{D1} represents the number of atoms of displaced alkanes and the N_{D2} represents the number of atoms of undisplaced alkanes remaining. The displacement efficiency can be calculated using the following formula:

$$E_D = N_{D1} / (N_{D1} + N_{D2}) \quad (6)$$

The calculation results of displacement efficiency in the five pore systems are shown in Fig. 11. Overall, the displacement efficiency of the inorganic pores is higher than that of the organic pore, and the displacement efficiency of CO₂ for octane is significantly higher than that of eicosane. The displacement efficiency of the four inorganic pores is very different. Comparing the feldspar system with high displacement efficiency and calcite with low displacement efficiency, the displacement efficiency of octane of the former is 1.77 times higher than that of the latter, and the displacement efficiency of eicosane is 4.70 times higher than that of the latter. The overall order of displacement efficiency is montmorillonite, feldspar > quartz > calcite > kerogen.

3.3. The effect of displacement velocity

Considering the significant influence of displacement velocity on CO₂ displacement behavior, a series of MD simulations are conducted to change the CO₂ displacement velocity. The above study shows that the CO₂ displacement effects of the four inorganic pore systems can be divided into two categories: the displacement effect of CO₂ in the pores of montmorillonite and feldspar is good, but the displacement effect of CO₂ in the pores of calcite and quartz is weak. In order to make the analysis clear and more targeted, kerogen pore, feldspar pore and calcite pore are selected as the research targets. The displacement velocity is set as 2, 4, 6 and 8 m/s, respectively, and the motion trajectory of alkanes at 8 nm is observed. From the simulation results, the displacement mechanism of CO₂ and shale oil at the molecular level could be obtained.

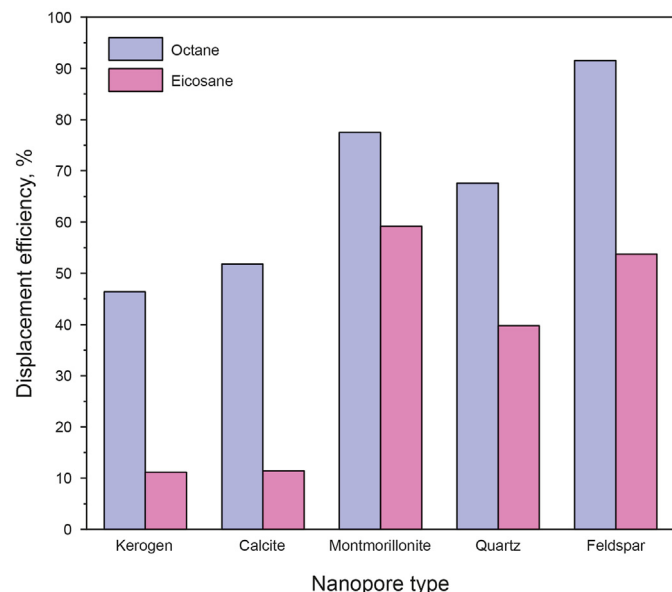


Fig. 11. The displacement efficiency of octane and eicosane in the pores.

As shown in Fig. 12, fluid motion states in the pores can be observed under different displacement velocities. When the displacement velocity is 2 m/s, the transport distance of alkanes in each pore is the longest, and the feldspar pore shows the most prominent performance. The white dashed line in the Fig. 12 represents the boundary at the exit end of the pore, and it can be seen that many octane molecules have been displaced out of the pore. It can also be observed that more alkanes are dissolved in the CO₂ slug in each pore at this time. This indicates that alkanes and CO₂ have good miscibility, which is conducive to the overall displacement of CO₂ for shale oil. With the increase in displacement velocity, the transport distance of alkanes in the pores decreases, and the residual number of alkanes on the porewall increases. It can be concluded that with the increase in CO₂ displacement velocity, the adsorption capacity of the porewall for CO₂ is decreased. It is difficult for CO₂ fluid to effectively displace and separate the alkanes on the porewall, and the residual oil layer formed by the porewall occupies the movement space of CO₂. Therefore, CO₂ tends to move away from the porewall, and the overall displacement capacity of alkanes is weakened. In addition, it is noteworthy that when the displacement velocity is 8 m/s, although the overall displacement length of the fluid is relatively short for the kerogen and calcite pore systems with relatively weak CO₂ displacement effect, the amount of residual oil near the pore entrance decreases significantly. It may be because at this time, the displacement rate is very high, and the driving force of CO₂ on the alkanes is increased, so the strong thrust generated on the alkanes forces them to move forward.

Fig. 13 shows the density distributions of octane and eicosane in the x direction in the three types of pores. When the displacement velocity is 2 m/s, for the kerogen and feldspar pores, compared with the displacement performance of 4 m/s previously analyzed, the density peaks of octane and eicosane are significantly shifted to the right, and the transport range of alkanes is increased. In addition, some alkanes are present at the pore outlet, which is not observed at 4 m/s. For the calcite pore, it is found that the density of octane near the entrance end of the pore decreases, while the density near the exit end of the pore increases. It indicates that the amount of residual octane on the porewall decreases and the number of octanes with high displacement distance increases. When the displacement velocity is 8 m/s, it can be directly observed that the density peaks of the two alkanes in all pores shift to the left, and the change degree of octane is greater. It is due to the better displacement effect and easier transport of octane than eicosane in the systems. The transport range of alkanes is reduced, which has the most obvious effect on the kerogen pore. The maximum transport distance of octane in x direction decreases from 15 nm at 2 m/s to 12.6 nm at 8 m/s, and eicosane decreases from 14.4 nm to 11.4 nm. In general, a lower displacement velocity is beneficial to CO₂ displacement behavior. When the displacement velocity increases, the displacement effect of CO₂ on alkanes is weakened, and the transport length of alkanes decreases.

The interaction energy in the system is calculated to study the energy difference between $E_{\text{ALKANES-CO}_2}$ and $E_{\text{ALKANES-WALL}}$, which is used to indicate the strength of CO₂ displacement ability for alkanes in the systems. When the value is less than 0, it indicates that the interaction between CO₂ and alkanes is stronger and the displacement ability is better. On the contrary, alkanes are more likely to be affected by the porewall surface, which is adsorbed on the porewall and not easy to be displaced. The calculation results are shown in Fig. 14(a), and the gray dotted line is the dividing line between the two interaction energies. With the increase in displacement velocity, the curves basically show a decreasing trend. For the feldspar and calcite pores, the value is always negative. It indicates that although the CO₂ displacement capacity

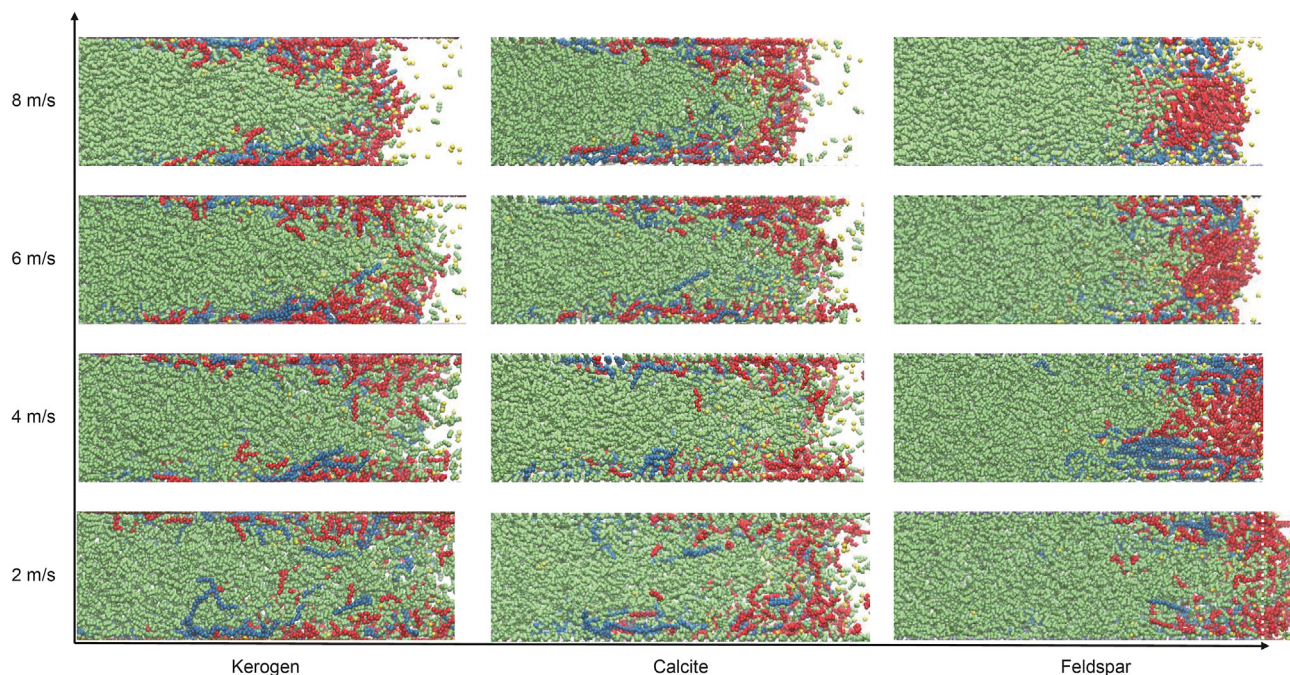


Fig. 12. Simulated snapshots in the three types of pores in the displacement process.

decreases with an increase in the velocity, the system can still maintain a good displacement effect. In contrast, the condition is satisfied only for a displacement velocity of 2 m/s in the case of kerogen pore. Therefore, for the kerogen pore, the displacement velocity has an important effect on CO₂ displacement behavior. Fig. 14(b) shows the transport distances of octane and eicosane in the *x* direction at different displacement velocities. It can also be found that with the increase in displacement velocity, the transport distance value in the *x* direction decreases. However, when the displacement velocity is 8 m/s, the curves in Fig. 14(a) and (b) both increase slightly, which is consistent with the analysis in Fig. 12.

The calculation results for the displacement efficiency of the two alkanes are shown in Fig. 15. As shown, as the displacement velocity is small, the displacement efficiency is relatively higher. As the displacement velocity increases, the values of displacement efficiency for the two alkanes decrease significantly. The declining degree is feldspar > calcite > kerogen, and the declining rate of octane is higher than that of eicosane. But once the displacement velocity is very high, as shown in the Fig. 15 at 8 m/s, the strong driving force can promote the alkane to move forward, and the displacement efficiency will recover slightly.

4. Conclusions

In this study, five different types of CO₂ displacement models are developed, including kerogen pore model and four types of inorganic pore models (quartz, feldspar, calcite and montmorillonite). A NEMD simulation method is used to address the CO₂ displacement behavior and displacement rule in shale nanopores. Based on the simulation results, the effect of displacement velocity and nanopore type on CO₂ displacement behavior is discussed. The main concluding remarks are as follows:

- (1) For the inorganic pores, the displacement effect of CO₂ on alkanes is significantly different, and the displacement efficiency of CO₂ for octane is significantly higher than that for eicosane. Compared with the heavy components in shale oil,

CO₂ has a better displacement effect on light components, and the light components have a longer transportation distance. The interaction energy between molecules has a great influence on the CO₂ displacement behavior in the pores. The interaction energy between alkanes and porewall surface in the calcite pores is stronger than that between shale oil and CO₂. It leads to an obvious CO₂ fingering phenomenon in the pore and finally a gas channeling process can be developed. Simultaneously, in comparison, the interaction energy between alkanes and porewall surface in the feldspar pores is reduced by about 5 times than that in the calcite pores. It indicates that a higher displacement efficiency can be obtained in the feldspar nanopores.

- (2) The displacement effect of CO₂ for alkanes in the organic pores is weaker than that in the inorganic pores. The peak density of octane in the organic pore is only 0.16 g/cm³, and the peak density in the other four inorganic pores is 0.18–0.30 g/cm³. The interaction energy between kerogen porewall and CO₂ is the smallest, which makes it the most difficult for CO₂ to separate and desorb the alkanes from kerogen porewall. The CO₂ displacement efficiency is shown as montmorillonite, feldspar > quartz > calcite > kerogen.
- (3) The lower displacement velocity makes alkanes and CO₂ have better miscibility, which is conducive to the overall displacement of CO₂ to shale oil. With the increase in displacement velocity, the transport distance of alkanes in the pores decreases, and the residual number of alkanes on the porewall increases. With the increase in displacement velocity, the displacement efficiency of alkanes will decrease significantly. But once the displacement velocity is very high, the strong driving force can promote the alkane to move forward, and the displacement efficiency will recover slightly. In comparison, the displacement efficiency of alkanes in feldspar nanopore can be increased by about 20% than that in the kerogen and calcite nanopores.

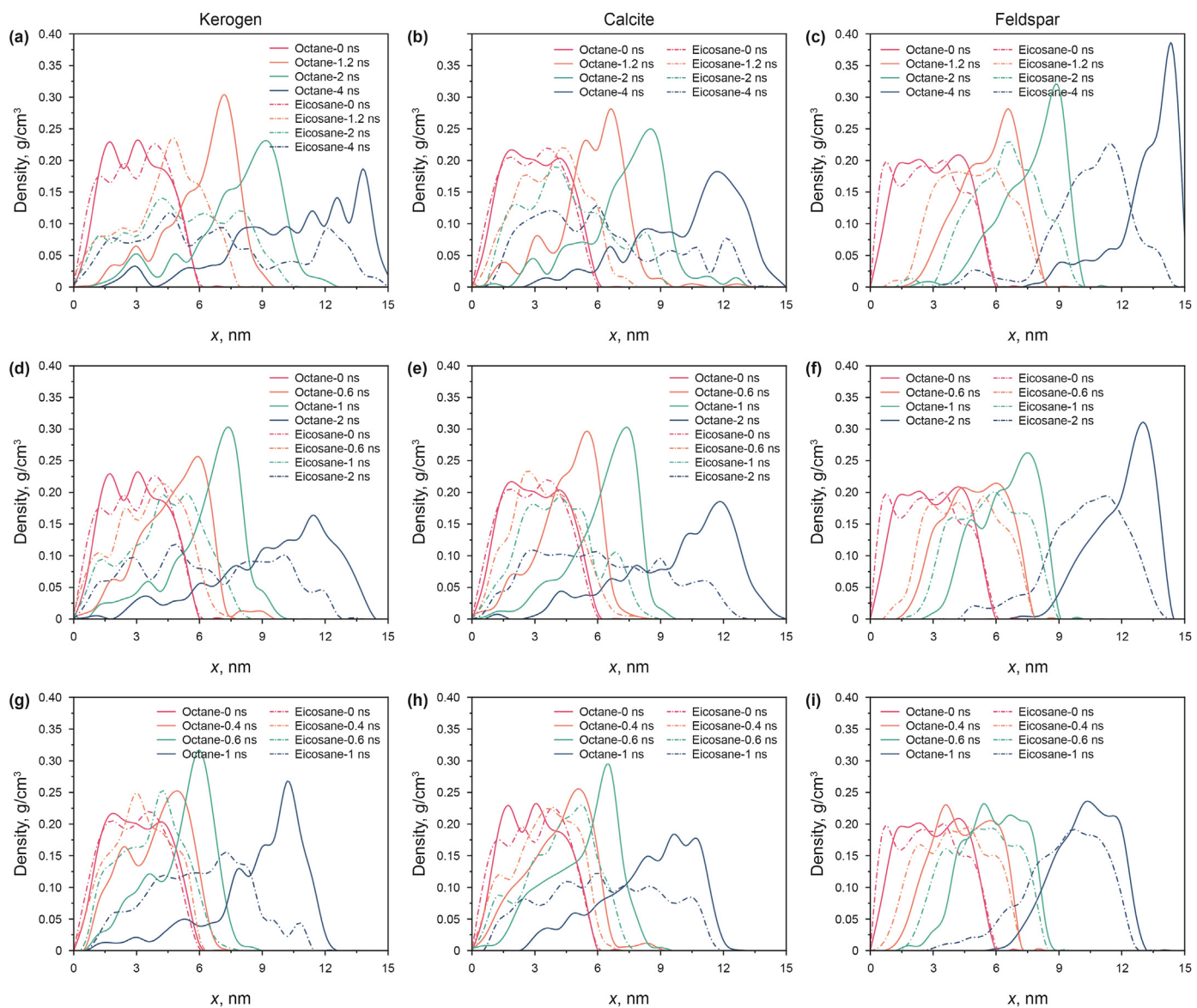


Fig. 13. Density distributions of alkanes at different displacement velocities of (a)–(c) 2 m/s, (d)–(f) 4 m/s, and (g–i) 8 m/s in three types of pores (kerogen (left), calcite (middle) and feldspar (right)).

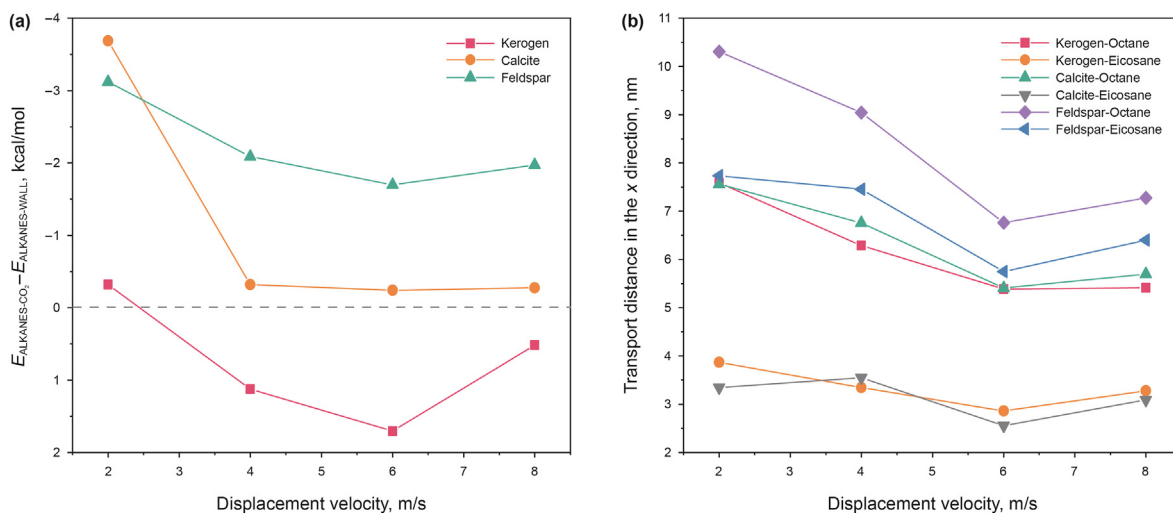


Fig. 14. (a) Distribution of interaction energy $E_{\text{ALKANES-CO}_2} - E_{\text{ALKANES-WALL}}$ in the systems; (b) Transport distances of alkanes in the x direction.

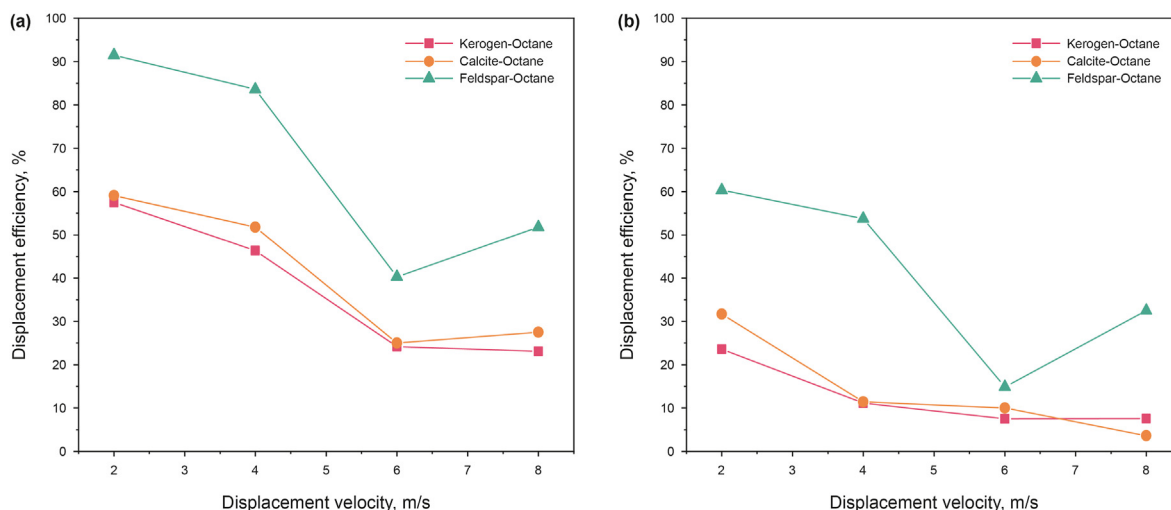


Fig. 15. Displacement efficiency of octane and eicosane in pores at different displacement velocities.

Declaration of competing interest

The authors declare that they have no known competing financial interests or personal relationships that could have appeared to influence the work reported in this paper.

Acknowledgements

This work was financially supported by the National Natural Science Foundation of China (No. 52004303) and Beijing Natural Science Foundation (No. 3212020).

References

- Agi, A., Junin, R., Abdullah, M.O., Jaafar, M.Z., Arsad, A., Sulaiman, W.R.W., Mohd Norddin, M.N.A., Abdurrahman, M., Abbas, A., Gbadamosi, A., Azli, N.B., 2020. Application of polymeric nanofluid in enhancing oil recovery at reservoir condition. *J. Petrol. Sci. Eng.* 194, 107476. <https://doi.org/10.1016/j.petrol.2020.107476>.
- Bousige, C., Ghimbeu, C.M., Vix-Guterl, C., Pomerantz, A.E., Suleimenova, A., Vaughan, G., Garbarino, G., Feygenson, M., Wildgruber, C., Ulm, F.-J., Pellenq, R.J.-M., Coasne, B., 2016. Realistic molecular model of kerogen's nanostructure. *Nat. Mater.* 15 (5), 576–582. <https://doi.org/10.1038/nmat4541>.
- Canneva, A., Giordana, I.S., Erra, G., Calvo, A., 2017. Organic matter characterization of shale rock by X-ray photoelectron spectroscopy: adventitious carbon contamination and radiation damage. *Energy Fuels* 31 (10), 10414–10419. <https://doi.org/10.1021/acs.energyfuels.7b01143>.
- Chaudhary, A.S., Ehlig-Economides, C., Wattenbarger, R., 2011. Shale oil production performance from a stimulated reservoir volume. In: SPE Annual Technical Conference and Exhibition. <https://doi.org/10.2118/147596-MS>.
- Chen, J., Yu, H., Fan, J., Wang, F., Lu, D., Liu, H., Wu, H., 2017. Channel-width dependent pressure-driven flow characteristics of shale gas in nanopores. *AIP Adv.* 7 (4), 045217. <https://doi.org/10.1063/1.4982729>.
- Chen, Z., Dong, X., Chen, Z., 2021. *n*-decane diffusion in carbon nanotubes with vibration. *J. Chem. Phys.* 154, 074505. <https://doi.org/10.1063/5.0038869>.
- Cygan, R.T., Liang, J.J., Kalinichev, A.G., 2004. Molecular models of hydroxide, oxyhydroxide, and clay phases and the development of a general force field. *J. Phys. Chem. B* 108 (4), 1255–1266. <https://doi.org/10.1021/jp0363287>.
- Dauber-Osguthorpe, P., Roberts, V.A., Osguthorpe, D.J., Wolff, J., Genest, M., Hagler, A.T., 1988. Structure and energetics of ligand binding to proteins: Escherichia coli dihydrofolate reductase-trimethoprim, a drug-receptor system. *Proteins: Struct., Funct., Bioinf.* 4 (1), 31–47. <https://doi.org/10.1002/prot.340040106>.
- Dong, X., Xu, W., Liu, R., Chen, Z., Lu, N., Guo, W., 2022. Insights into adsorption and diffusion behavior of shale oil in slit nanopores: a molecular dynamics simulation study. *J. Mol. Liq.* 359, 119322. <https://doi.org/10.1016/j.molliq.2022.119322>.
- Dong, X., Xu, W., Liu, H., Chen, Z., Lu, N., Wang, W., 2023. On the replacement behavior of CO₂ in nanopores of shale oil reservoirs: insights from wettability tests and molecular dynamics simulations. *Geoenergy Sci. Eng.* 223, 211528. <https://doi.org/10.1016/j.geoen.2023.211528>.
- Etha, S.A., Desai, P.R., Sachar, H.S., Das, S., 2021. Wetting dynamics on solvophilic,

- soft, porous, and responsive surfaces. *Macromolecules* 54 (2), 584–596. <https://doi.org/10.1021/acs.macromol.0c02234>.
- Fan, L., Chen, J., Zhu, J., Nie, X., Li, B., Shi, Z., 2022. Experimental study on enhanced shale oil recovery and remaining oil distribution by CO₂ flooding with nuclear magnetic resonance technology. *Energy Fuels* 36 (4), 1973–1985. <https://doi.org/10.1021/acs.energyfuels.1c02982>.
- Fang, T., Wang, M., Wang, C., Liu, B., Shen, Y., Dai, C., Zhang, J., 2017. Oil detachment mechanism in CO₂ flooding from silica surface: molecular dynamics simulation. *Chem. Eng. Sci.* 164, 17–22. <https://doi.org/10.1016/j.ces.2017.01.067>.
- Fang, T., Zhang, Y., Ding, B., Yan, Y., Zhang, J., 2020. Static and dynamic behavior of CO₂ enhanced oil recovery in nanoslits: effects of mineral type and oil components. *Int. J. Heat Mass Tran.* 153, 119583. <https://doi.org/10.1016/j.ijheatmasstransfer.2020.119583>.
- Feng, Q., Xu, S., Xing, X., Zhang, W., Wang, S., 2020. Advances and challenges in shale oil development: a critical review. *Adv. Geo-Energy Res.* 4 (4), 406–418. <https://doi.org/10.46690/ager.2020.04.06>.
- Goumans, T.P.M., Wander, A., Brown, W.A., Catlow, C.R.A., 2007. Structure and stability of the (0 0 1) α -quartz surface. *Phys. Chem. Chem. Phys.* 9 (17), 2146–2152. <https://doi.org/10.1039/B701176H>.
- Han, M.L., Wei, X.L., Zhang, J.C., Liu, Y., Tang, X., Li, P., Liu, Z.Y., 2022. Influence of structural damage on evaluation of microscopic pore structure in marine continental transitional shale of the Southern North China Basin: a method based on the low-temperature N₂ adsorption experiment. *Petrol. Sci.* 19 (1), 100–115. <https://doi.org/10.1016/j.petsci.2021.10.016>.
- Hoffman, B.T., Shoab, S., 2014. CO₂ flooding to increase recovery for unconventional liquids-rich reservoirs. *J. Energy Resour. Technol.* 136 (2), 022801. <https://doi.org/10.1115/1.4025843>.
- Hu, M., Cheng, Z., Zhang, M., Liu, M., Song, L., Zhang, Y., Li, J., 2014. Effect of calcite, kaolinite, gypsum, and montmorillonite on Huadian oil shale kerogen pyrolysis. *Energy Fuels* 28 (3), 1860–1867. <https://doi.org/10.1021/ef4024417>.
- Huang, X., Tian, Z., Zuo, X., Li, X., Yang, W., Lu, J., 2023. The microscopic pore crude oil production characteristics and influencing factors by DME-assisted CO₂ injection in shale oil reservoirs. *Fuel* 331, 125843. <https://doi.org/10.1016/j.fuel.2022.125843>.
- Jia, B., Tsau, J.S., Barati, R., 2019. A review of the current progress of CO₂ injection EOR and carbon storage in shale oil reservoirs. *Fuel* 236, 404–427. <https://doi.org/10.1016/j.fuel.2018.08.103>.
- Jorgensen, W.L., Madura, J.D., Swenson, C.J., 1984. Optimized intermolecular potential functions for liquid hydrocarbons. *J. Am. Chem. Soc.* 106 (22), 6638–6646. <https://doi.org/10.1021/ja00334a030>.
- Kerisit, S., Liu, C., 2012. Diffusion and adsorption of uranyl carbonate species in nanosized mineral fractures. *Environ. Sci. Technol.* 46 (3), 1632–1640. <https://doi.org/10.1021/es2027696>.
- Kovscek, A.R., Tang, G.Q., Vega, B., 2008. Experimental investigation of oil recovery from siliceous shale by CO₂ injection. In: SPE Ann. Techn. Conf. Exhib. <https://doi.org/10.2118/115679-MS>.
- Li, H.B., Yang, Z.M., Li, R.S., Zhou, T.Y., Guo, H.K., Liu, X.W., Dai, Y.X., Hu, Z.G., Meng, H., 2021. Mechanism of CO₂ enhanced oil recovery in shale reservoirs. *Petrol. Sci.* 18 (6), 1788–1796. <https://doi.org/10.1016/j.petsci.2021.09.040>.
- Li, X., Wang, P., Yan, Z., Yu, S., Wei, K., Zhu, X., Xue, Q., 2022. The miscible behaviors of C₃H₈/C₃H₁₈ (C₇H₁₇N) system in nanoslits: effects of pore size and rock surface wettability. *Chem. Eng. J.* 431, 133988. <https://doi.org/10.1016/j.cej.2021.133988>.
- Li, Z., Yao, J., Ren, Z., Sun, H., Zhang, L., Yang, Y., Fan, T., Kou, J., 2019. Accumulation behaviors of methane in the aqueous environment with organic matters. *Fuel* 236, 836–842. <https://doi.org/10.1016/j.fuel.2018.09.071>.
- Liu, H., Tao, J., Meng, S., Li, D., Cao, G., Gao, Y., 2022a. Application and prospects of

- CO₂ enhanced oil recovery technology in shale oil reservoir. *China Petrol. Explor.* 27 (1), 127–134. <https://doi.org/10.3969/j.issn.1672-7703.2022.01.012> (in Chinese).
- Liu, B., Wang, C., Zhang, J., Xiao, S., Zhang, Z., Shen, Y., Sun, B., He, J., 2017. Displacement mechanism of oil in shale inorganic nanopores by supercritical carbon dioxide from molecular dynamics simulations. *Energy Fuels* 31 (1), 738–746. <https://doi.org/10.1021/acs.energyfuels.6b02377>.
- Liu, S.Y., Ren, B., Li, H.Y., Yang, Y.Z., Wang, Z.Q., Wang, B., Agarwal, R., 2022b. CO₂ storage with enhanced gas recovery (CSEGR): a review of experimental and numerical studies. *Petrol. Sci.* 19 (2), 594–607. <https://doi.org/10.1016/j.petsci.2021.12.009>.
- Liu, X., Zhang, D., 2019. A review of phase behavior simulation of hydrocarbons in confined space: implications for shale oil and shale gas. *J. Nat. Gas Sci. Eng.* 68, 102901. <https://doi.org/10.1016/j.jngse.2019.102901>.
- Liu, Y., Wilcox, J., 2012. Effects of surface heterogeneity on the adsorption of CO₂ in microporous carbons. *Environ. Sci. Technol.* 46 (3), 1940–1947. <https://doi.org/10.1021/es204071g>.
- Loucks, R.G., Reed, R.M., Ruppel, S.C., Jarvie, D.M., 2009. Morphology, genesis, and distribution of nanometer-scale pores in siliceous mudstones of the Mississippian Barnett Shale. *J. Sediment. Res.* 79 (12), 848–861. <https://doi.org/10.2110/jsr.2009.092>.
- Meyer, J.C., Geim, A.K., Katsnelson, M.I., Novoselov, K.S., Booth, T.J., Roth, S., 2007. The structure of suspended graphene sheets. *Nature* 446 (7131), 60–63. <https://doi.org/10.1038/nature05545>.
- Prieve, D.C., Russel, W.B., 1988. Simplified predictions of Hamaker constants from Lifshitz theory. *J. Colloid Interface Sci.* 125 (1), 1–13. [https://doi.org/10.1016/0021-9797\(88\)90048-3](https://doi.org/10.1016/0021-9797(88)90048-3).
- Safi, R., Agarwal, R.K., Banerjee, S., 2016. Numerical simulation and optimization of CO₂ utilization for enhanced oil recovery from depleted reservoirs. *Chem. Eng. Sci.* 144, 30–38. <https://doi.org/10.1016/j.ces.2016.01.021>.
- Shaw, D.B., Weaver, C.E., 1965. The mineralogical composition of shales. *J. Sediment. Res.* 35 (1), 213–222. <https://doi.org/10.1306/74D71221-2B21-11D7-8648000102C1865D>.
- Soni, A., Patey, G.N., 2019. Simulations of water structure and the possibility of ice nucleation on selected crystal planes of K-feldspar. *J. Chem. Phys.* 150 (21), 214501. <https://doi.org/10.1063/1.5094645>.
- Sun, J., Chen, Z., Wang, X., Zhang, Y., Qin, Y., Chen, C., Li, W., Zhou, W., 2023. Displacement characteristics of CO₂ to CH₄ in heterogeneous surface slit pores. *Energy Fuels* 37 (4), 2926–2944. <https://doi.org/10.1021/acs.energyfuels.2c03610>.
- Ungerer, P., Collett, J., Yiannourakou, M., 2015. Molecular modeling of the volumetric and thermodynamic properties of kerogen: influence of organic type and maturity. *Energy Fuels* 29 (1), 91–105. <https://doi.org/10.1021/ef502154k>.
- Wang, L., Parsa, E., Gao, Y., Ok, J.T., Neeves, K., Yin, X., Ozkan, E., 2014. Experimental study and modeling of the effect of nanoconfinement on hydrocarbon phase behavior in unconventional reservoirs. In: SPE Western North American and Rocky Mountain Joint Meeting. <https://doi.org/10.2118/169581-MS>.
- Wang, Q., Ye, J.B., Yang, H.Y., Liu, Q., 2016b. Chemical composition and structural characteristics of oil shales and their kerogens using Fourier Transform Infrared (FTIR) spectroscopy and solid-state ¹³C Nuclear Magnetic Resonance (NMR). *Energy Fuels* 30 (8), 6271–6280. <https://doi.org/10.1021/acs.energyfuels.6b00770>.
- Wang, S., Feng, Q., Zha, M., Lu, S., Qin, Y., Xia, T., Zhang, C., 2015. Molecular dynamics simulation of liquid alkane occurrence state in pores and slits of shale organic matter. *Petrol. Explor. Dev.* 42 (6), 844–851. [https://doi.org/10.1016/S1876-3804\(15\)30081-1](https://doi.org/10.1016/S1876-3804(15)30081-1).
- Wang, S., Javadpour, F., Feng, Q., 2016a. Fast mass transport of oil and supercritical carbon dioxide through organic nanopores in shale. *Fuel* 181, 741–758. <https://doi.org/10.1016/j.fuel.2016.05.057>.
- Wang, X., Huang, X., Lin, K., Zhao, Y.P., 2019. The constructions and pyrolysis of 3D kerogen macromolecular models: experiments and simulations. *Glob. Chall.* 3 (5), 1900006. <https://doi.org/10.1002/gch2.201900006>.
- Wang, X., Luo, P., Er, V., Huang, S., 2010. Assessment of CO₂ flooding potential for bakken formation, Saskatchewan, In: Can. Unconvent. Resour. Int. Petrol. Conf. <https://doi.org/10.2118/137728-MS>.
- Wei, B., Zhang, X., Liu, J., Xu, X., Pu, W., Bai, M., 2020. Adsorptive behaviors of supercritical CO₂ in tight porous media and triggered chemical reactions with rock minerals during CO₂-EOR and-sequestration. *Chem. Eng. J.* 381, 122577. <https://doi.org/10.1016/j.cej.2019.122577>.
- Wu, T., Zhang, D., 2016. Impact of adsorption on gas transport in nanopores. *Sci. Rep.* 6 (1), 23629. <https://doi.org/10.1038/srep23629>.
- Xiao, S., Edwards, S.A., Gräter, F., 2011. A new transferable forcefield for simulating the mechanics of CaCO₃ crystals. *J. Phys. Chem. C* 115 (41), 20067–20075. <https://doi.org/10.1021/jp202743v>.
- Xiong, C., Li, S., Ding, B., Geng, X., Zhang, J., Yan, Y., 2021. Molecular insight into the oil displacement mechanism of gas flooding in deep oil reservoir. *Chem. Phys. Lett.* 783, 139044. <https://doi.org/10.1016/j.cplett.2021.139044>.
- Xu, T., Hoffman, T., 2013. Hydraulic fracture orientation for miscible gas injection EOR in unconventional oil reservoirs. In: SPE/AAPG/SEG Unconventional Resources Technology Conference. <https://doi.org/10.1190/urtec2013-189>.
- Yan, Y., Li, C., Dong, Z., Fang, T., Sun, B., Zhang, J., 2017. Enhanced oil recovery mechanism of CO₂ water-alternating-gas injection in silica nanochannel. *Fuel* 190, 253–259. <https://doi.org/10.1016/j.fuel.2016.11.019>.
- Yang, L., Jin, Z., 2019. Global shale oil development and prospects. *China Petrol. Explor.* 24 (5), 553. <https://doi.org/10.3969/j.issn.1672-7703.2019.05.002> (in Chinese).
- Yang, M., Stipp, S.S., Harding, J., 2008. Biological control on calcite crystallization by polysaccharides. *Cryst. Growth Des.* 8 (11), 4066–4074. <https://doi.org/10.1021/cg300772h>.
- Yu, H., Fan, J., Xia, J., Liu, H., Wu, H., 2020a. Multiscale gas transport behavior in heterogeneous shale matrix consisting of organic and inorganic nanopores. *J. Nat. Gas Sci. Eng.* 75, 103139. <https://doi.org/10.1016/j.jngse.2019.103139>.
- Yu, H., Xu, H., Xia, J., Fan, J., Wang, F., Wu, H., 2020b. Nanoconfined transport characteristic of methane in organic shale nanopores: the applicability of the continuous model. *Energy Fuels* 34 (8), 9552–9562. <https://doi.org/10.1021/acs.energyfuels.0c01789>.
- Zhang, Q., Su, Y., Wang, W., Lu, M., Sheng, G., 2017. Apparent permeability for liquid transport in nanopores of shale reservoirs: coupling flow enhancement and near wall flow. *Int. J. Heat Mass Tran.* 115, 224–234. <https://doi.org/10.1016/j.ijheatmasstransfer.2017.08.024>.
- Zhang, W., Feng, Q., Wang, S., Xing, X., 2019. Oil diffusion in shale nanopores: insight of molecular dynamics simulation. *J. Mol. Liq.* 290, 111183. <https://doi.org/10.1016/j.molliq.2019.111183>.
- Zhang, Y., Fang, T., Ding, B., Wang, W., Yan, Y., Li, Z., Guo, W., Zhang, J., 2020. Migration of oil/methane mixture in shale inorganic nano-pore throat: a molecular dynamics simulation study. *J. Petrol. Sci. Eng.* 187, 106784. <https://doi.org/10.1016/j.petrol.2019.106784>.
- Zhou, W., Jiang, L., Liu, X., Hu, Y., Yan, Y., 2022. Molecular insights into the effect of anionic-nonionic and cationic surfactant mixtures on interfacial properties of oil-water interface. *Colloids Surf. A Physicochem. Eng. Asp.* 637, 128259. <https://doi.org/10.1016/j.colsurfa.2022.128259>.
- Zhou, X., Yuan, Q., Zhang, Y., Wang, H., Zeng, F., Zhang, L., 2019. Performance evaluation of CO₂ flooding process in tight oil reservoir via experimental and numerical simulation studies. *Fuel* 236, 730–746. <https://doi.org/10.1016/j.fuel.2018.09.035>.